Review of Photonic Integrated Optical Phased Arrays for Space Optical Communication

JINGWEN HE, TAO DONG, AND YUE XU

State Key Laboratory of Space-Ground Integrated Information Technology, Beijing Institute of Satellite Information Engineering, Beijing 100095, China

Corresponding author: Tao Dong (dongtaoandy@163.com)

ABSTRACT A review of photonic integrated optical phased array (OPA) for space optical communication is presented. We review and summarize the typical works of the photonic integrated OPAs with one-dimensional and two-dimensional optical antenna array in recent years. The basic components of the photonic integrated OPA are introduced separately, including optical coupler, optical power division network, phase shifter, and optical antenna. In addition, the configuration of the optical antenna array and the control circuit are introduced for OPA beam steering. The basic principle and experiment setup for testing the radiation properties of the OPA are presented. A proof-of-concept nonuniform silicon integrated OPA with 64 antennas is designed and a one-dimensional beam steering range of 28° is achieved with beam width of about 0.25°. The challenges and development trends of large-scale integrated OPA chip applied in space optical communication are also discussed.

INDEX TERMS Beam steering, large scale, optical phased array, photonic integration, space optical communication.

I. INTRODUCTION

Recently, radio frequency (RF) communication has been widely used in our daily life, but the communication speed is low and cannot reach to a few Gbps. With the demand of large-capacity and high-speed communication, the communication frequency gradually expands to high frequency. Space optical communication possesses significant advantages of large communication capacity, convenient networking, concentrated energy and good security. With the rapid growth of satellite-to-ground and inter-satellite transmission bandwidth requirements, space optical communication will be an important means of high-speed inter-satellite communication and networking. The current satellite-borne laser communication terminal achieves acquisition, tracking and pointing (ATP) by using the mechanic servo and optical lens, but this method has some shortcomings, such as low steering speed, no beam agility, large volume and heavy weight. In the practical application of low earth orbit (LEO) satellite network with inter-satellite links, one of the satellite nodes of inter-satellite laser communication network needs to establish at least four links with its neighbors. As shown in Fig. 1, four links between LEO satellite A and its neighboring satellites B, C, D, and E are established, which include two links with satellite nodes in the same orbit and other two links with satellite nodes in

The associate editor coordinating the review of this manuscript and approving it for publication was Davide Ramaccia.
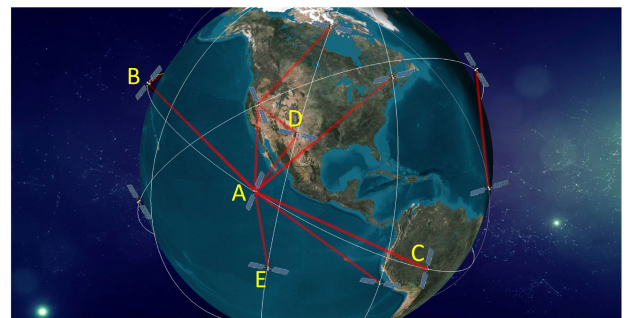

FIGURE 1. Inter-satellite laser communication network for low earth orbit (LEO) satellites.

different orbits. Due to the limitation of heavy weight and large volume of the mechanical servo and optical lens, the traditional beam-steering system cannot meet the requirement of inter-satellite networking for fast establishment of multiple links simultaneously.

In recent years, optical phased array (OPA) has received increasing interest as a non-mechanical beam-steering device. OPA is an optical antenna array with adjustable phase, whose operating principle is similar to microwave phased array, and it performs beam steering by controlling the phase of light radiated by each optical antenna without mechanical servo system. Compared with the traditional optical communication terminal, OPA has the advantages of high steering

TABLE 1. Inter-satellite Link Budget for Two Neighboring LEO Satellites Distance of 2000 km

Parameter	Typical Value	Unit
Transmission power	26	dBm
Geometric loss[a](Distance loss)	-52	dB
Receiver loss[b]	-3	dB
Receiver sensitivity[c]	-45	dBm
Link margin[d]	16	dB

[a]Geometric loss formula: $\frac{P_r}{P_t}=\left(\frac{\pi D_r D_t}{4\lambda R}\right)^2$, P_r and P_t are the received and transmitted power, D_r and D_t are the receiver and transmitter apertures (0.1 m), λ is the wavelength (1.55 μm), and R is the distance (2000 km). The approximate power ratio is $\sim$ -58 dB. Considering the optical antenna receiving efficiency (-1 dB), the geometric loss is $\sim$ -52 dB.

[b]Receiver loss is the coupling loss for coupling space light into single mode fiber.

[c]Receiver sensitivity: the receiver sensitivity of 10 Gbps single-polarization QPSK coherent optical communication is $\sim$ -45 dBm according to the experiment result [1].

[d]Link margin formula: Link margin = Transmission power + Geometric loss + Receiver loss - Receiver sensitivity.

speed, beam agility, multi-beam steering, small size and light weight, so it can be used as a candidate for further realizing the inter-satellite communication network and increasing the flexibility of the network. Generally, the distance between two neighboring typical LEO satellites is about 2000 km. For an OPA with transmit and receive aperture of 0.1 m, if the transmission rate is 10 Gbps, then the transmission power should be about 26 dBm. Specifically, the link budget formula is used to calculate the link budget, and the parameters such as transmitting antenna aperture (gain), transmission power, receiving antenna aperture (gain), receiver sensitivity, geometric loss, and receiver loss are considered, and meanwhile, a 16 dB link margin is reserved. The inter-satellite link budget is listed in Table 1. It means that when the optical power radiated by OPA reaches 400 mW, the applicability demand of the space optical communication will be satisfied.

OPA can be realized in different ways, such as liquid crystal [2]–[4], micro-electromechanical system (MEMS) [5]–[8], and photonic integrated circuit (PIC). OPA based on liquid crystal realizes optical beam steering by altering the voltage loaded on the crystal molecules. The phase of electromagnetic (EM) wave is controlled by changing the orientation of liquid crystal molecule, which is controlled by external electric field. However, the beam steering speed and steering range of the liquid crystal based OPA are limited. OPA based on MEMS realizes beam steering by vibration of the steering mirrors. However, MEMS has some weaknesses, such as small steering range, low steering speed, and high power consumptions. Generally, beam steering range of OPA based on MEMS does not exceed 10° [5]–[8]. Comparing with MEMS based OPA, photonic integrated OPA has better stability and larger beam steering range. Photonic integrated OPA is proposed to integrate all the necessary components, including light source, power splitters, amplifiers, phase shifters, and optical antennas on a single chip by utilizing the complementary metal-oxide-semiconductor

(CMOS) process. By using the phase shifters, photonic integrated OPA can realize high-speed beam steering of at least 1 MHz in free space. In general, the modulation speed of a thermo-optic phase shifter is about 1 MHz. In order to achieve a higher beam steering speed, the electro-optic phase shifter will be used, whose modulation speed is more than 1 GHz. The traditional optical communication terminal achieves beam steering by mechanical servo combined with optical lenses, and the beam steering speed is about 1 KHz. By comparing with the traditional beam steering method, the beam steering speed of photonic integrated OPA is at least three orders of magnitude higher. Nowadays, the optical communication terminals on LEO satellites using mechanical servo and optical lenses have realized inter-satellite optical communication. If the speed of communication link building and switching becomes higher, the network flexibility will be increased, so as to improve the user experience. Therefore, photonic integrated OPA has the potential to realize chip-scale system for beam steering, and to reduce the cost of the communication terminal applied in space optical communication.

In this paper, we present a review of the development of the photonic integrated OPA and introduce in detail the key components of the photonic integrated OPA. The rest of this paper is organized as follows. In Section II, a review of the research development of photonic integrated OPA in recent years is given. Section III introduces the key components of the OPA, including optical coupler, optical power division network, phase shifter, optical antenna, optical antenna array, and control circuit. The far-field radiation properties of OPA and experiment setup of OPA test are introduced in Section IV. In Section V, as a proof-of-concept, a silicon integrated OPA with 1×64 nonuniform antenna array is designed and its far-field radiation properties are investigated in detail. The conclusions and prospects are given in Section VI.

II. REVIEW OF THE DEVELOPMENT OF PHOTONIC INTEGRATED OPA

In recent years, photonic integrated OPA has been extensively researched. In terms of antenna arrangement, the existing photonic integrated OPAs are divided into one-dimensional (1D) and two-dimensional (2D) OPAs. For 1D OPA, optical antennas are arranged in one certain direction on the substrate. For 2D OPA, optical antennas are arranged along two different directions in the same plane. An overview of the development of the photonic integrated OPA is summarized as follows, and the measured performance of the fabricated OPAs is listed in Table 2 in detail.

A. PHOTONIC INTEGRATED OPAS WITH 1D ANTENNA ARRAY

The first photonic integrated monolithic OPA was proposed by K. V. Acoleyen *et al.* in 2009 [9]. As shown in Fig. 2(a), the OPA chip consists of a 1×16 waveguide grating antenna array and is fabricated on silicon-on-insulator (SOI). At 1550 nm, a beam steering of 2.3° in the direction perpendicular to the waveguide gratings ψ is realized by using 16 thermo-optic

TABLE 2. Photonic Integrated OPAs

Process technology	# of emitters	Array dimension	Steering range	Beam width	Radiation	Amplitude weighting	Year	Institute
Si	1×16	1D	2.3°	N/A	broadside	No	2009	UGent [9]
InP	1×8	1D	10°	N/A	broadside	Yes	2013	UCSB [14]
III-V/Si	1×32	1D	23°	1°	broadside	Yes	2015	UCSB [15]
Si	1×50	1D	46°	0.85°	broadside	No	2016	MIT [10]
Si	128	1D	80°	0.14°	broadside	No	2016	Intel [11]
Si	1×1024	1D	45°	0.03°	broadside	No	2017	USC [12]
Si	1×512	1D	70°	0.15°	broadside	No	2018	CC [13]
Si	1×64	1D	180°	1.6°	end-fire	No	2018	CC [17]
Si	8×8	2D	6°×6°	N/A	broadside	No	2013	MIT [19]
Si	8×8	2D	1.6°×1.6°	N/A	broadside	Yes	2015	USC [20]
Si	8×8	2D	7°×7°	N/A	broadside	No	2019	UPenn [21]
Si	128	2D	16°×16°	0.8°×0.8°	broadside	No	2019	CIT [22]
3D Si	4×4	2D	4.93°×4.93°	N/A	end-fire	No	2015	UCD [24]
3D Si	16×16	2D	N/A	N/A	end-fire	No	2016	UCD [25]

phase shifters and a beam steering of 14.1° in the direction along the waveguide gratings θ is realized by changing the wavelength from 1500 nm to 1600 nm. Since then, some studies related to 1D OPA have been published, and the scale of the optical antenna array in the OPA chip has also been expanded [10]–[12].

With the increase of the number of antennas, it will face various challenges, such as the increased number of phase shifters, huge power consumption, and the complexity of the control circuit. In 2017, Chung *et al.* proposed a scalable architecture by introducing sub-array concept and sharing control electronics among multiple phase shifters [12]. Based on this scheme, an integrated OPA with 1 × 1024 antennas, the largest number of antennas so far, has been demonstrated as shown in Fig. 2(b), and beam steering range of 45° has been achieved with a narrow beam width of 0.03°. This scheme can greatly reduce the number of electronic components and power consumption, but the beam control accuracy is limited because not all phase shifters are controlled independently in the OPA. Using the phase shifters with high efficiency is another alternative approach to realize a large-scale OPA. S. A. Miller *et al.* have proposed a low-power multipass phase shifter structure, whose power consumption was reduced to 1.7 mW/pi [13]. On the basis of this kind of multi-pass phase shifter, they have demonstrated a low-power 1 × 512 silicon integrated OPA with 512 independently controllable phase shifters. By adjusting the phase shifter and wavelength of the incident light respectively, 2D beam steering range of 70° × 6° with a beam width of 0.15° × 0.15° is obtained, and the array power consumption is only about 1.9 W, which is much lower than that of the OPAs with traditional thermo-optic phase shifters.

The silicon integrated OPAs have been demonstrated using off-chip laser sources. To improve the reliability of the chip and avoid the fiber coupling loss, the scheme of integrating the laser sources into the OPA chip is proposed. Due to the direct bandgap and high quantum efficiency of the InP material, InP-based PIC is widely used to achieve on-chip light sources and amplifiers. With the advancement of III-V heterogeneous integration technologies, laser diodes and optical amplifiers can be integrated on the same OPA chip [14], [15]. Fig. 2(c) shows the layout of an InP photonic integrated 1 × 8 OPA including on-chip tunable laser, semiconductor optical amplifiers (SOAs), splitters, phase shifters, emission array, and detectors [14]. Similarly, another fully-integrated OPA chip with 1 × 32 antenna array was implemented by using the hybrid III-V/silicon platform [15]. As shown in Fig. 2(d), the OPA chip not only contains the key components, but also adds a photonic crystal lens for imaging and coupling the far field to the photodiode array for on-chip feedback. The photonic integrated OPA exhibited a 2D beam steering over 23° × 3.6° with beam width of 1° × 0.6°. In recent years, 3D PICs have been emerged as very important way towards bringing new microsystems. Generally, some 3D PICs are formed by ultrafast laser inscription, and some others are formed by stacking multiple 2D PIC layers. In order to improve the utilization of the chip area, an 1 × 120 ultra-compact OPA with vertical U-turn interlayer coupling structures was proposed and implemented by utilizing 3D PIC technology [16]. As shown in Fig. 2(e), the OPA chip consists of two layers optically interconnected by a vertical U-turn structure. The top layer is the emitting layer with optical antenna array, and the bottom layer is the active photonic layer with phase shifters, amplifiers, etc.

The OPA chips mentioned above radiate beams upward with the grating antennas in chip, which are called broadside OPA. End-fire OPA is another type of OPA architecture, which radiates beams forward with waveguides directly. Fig. 2(f) displays the optical image of an end-fire OPA chip bonded on the printed circuit board (PCB) [17]. The designed
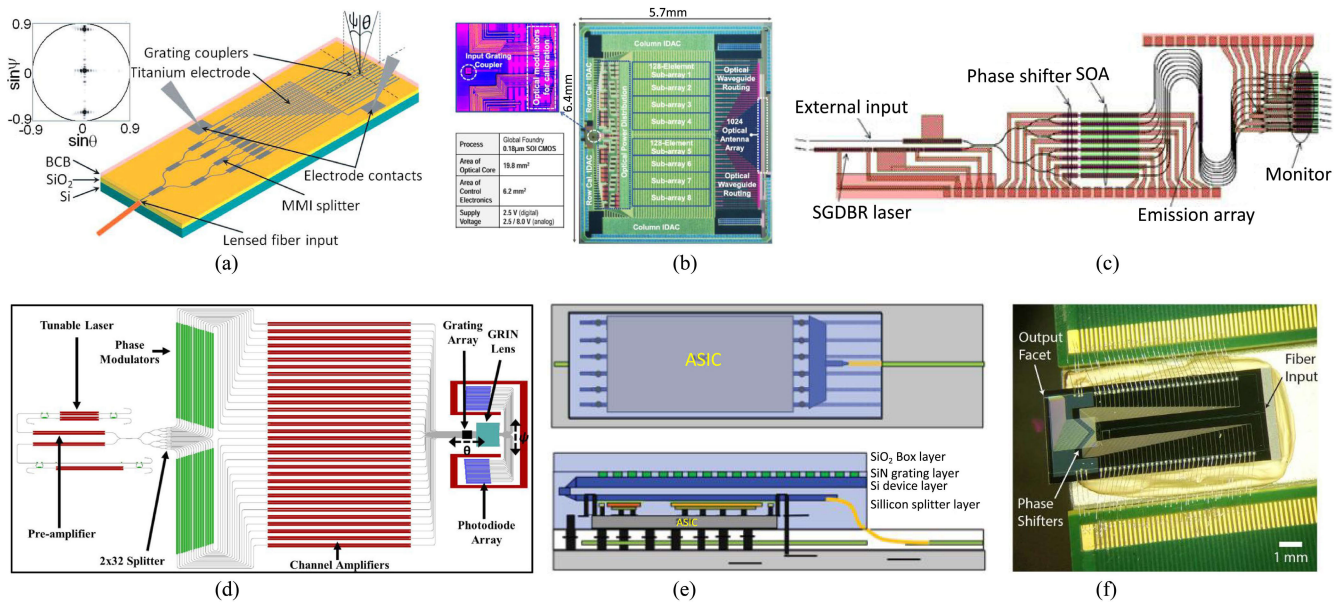
FIGURE 2. Design schemes of 1D OPA. (a) Schematic of the Diagram of the photonic integrated monolithic OPA chip with 1 × 16 grating antennas [9]. (b) Microphotograph of the 1 × 1024 OPA chip [12]. (c) Layout of the InP photonic integrated 1 × 8 OPA with on-chip tunable laser [14]. (d) Layout of the fully-integrated 1 × 32 OPA chip [15]. (e) Perspective schematic of the 1 × 120 ultra-compact OPA with vertical U-turn interlayer coupling structures [16]. (f) Optical image of the end-fire OPA chip bonded on the printed circuit board (PCB) [17].

OPA does not include the optical antenna array, and the beam is radiated from the end face of the chip with 64 waveguides. The waveguide spacing is half-wavelength, and the crosstalk between each waveguide is eliminated by designing phase mismatch between neighboring waveguides. Due to the small distance between the emitters, a wide beam steering range of 180° with beam width of 1.6° is achieved.

For 1D OPA, beam steering in two orthogonal directions is achieved by phase shifter operating in the array dimension and wavelength tuning in the antenna dimension, respectively. Generally, the beam steering range achieved by wavelength tuning is relatively small. In fact, a variable wavelength is not suitable for space optical communication. The 1D OPA cannot realize 2D phase-controlled beam steering. Therefore, 1D photonic integrated OPA cannot meet the application requirements of inter-satellite communication networking. In order to achieve a 2D beam steering by phase controlling, it is essential to develop the research of 2D OPA.

B. PHOTONIC INTEGRATED OPAS WITH 2D ANTENNA ARRAY

The original 2D OPAs do not contain phase shifters, and the beam steering cannot be realized by phase control [18, 19]. Dynamic beam steering and shaping can be achieved by adding phase shifters in the waveguides. An 8 × 8 silicon integrated OPA with 64 thermo-optic phase shifters was demonstrated, and the light was evenly distributed to the S-shaped waveguide with a thermo-optic phase shifter by using a series optical power division network, as shown in Fig. 3(a) [19]. By active phase tuning, a beam steering range of 6° in both the vertical direction and the horizontal direction is achieved. Furthermore, another 8 × 8 monolithic OPA that integrates tunable attenuators and control

electronics on the same substrate was fabricated by using the CMOS SOI process [20]. The schematic of the monolithic OPA and the chip microphotograph of the fabricated OPA including over 300 optical components and over 74000 electrical components are shown in Fig. 3(b). In these two kinds of 8 × 8 silicon integrated OPAs, the series optical power division network is adopted, which can be easily extended in two orthogonal directions. However, due to the phase shifters included in the antenna array, the antenna spacing cannot be further reduced, which will limit the beam steering range of the OPA. In order to obtain an optical antenna array with compact antenna spacing and reduce the number of phase shifters and the electric power consumption, the approach of sharing phase shifters can also be used in the 2D OPA. For example, in the 8×8 OPA shown in Fig. 3(c), 16 phase shifters are placed outside of the antenna array by utilizing the parallel optical power division network, and a 2D beam steering in the range of 7° × 7° is achieved [21]. Similarly, a larger 2D OPA with 128 antennas was proposed, and a large beam steering range of 16° × 16° with the beam width of 0.8° × 0.8° was realized by designing a nonuniform sparse antenna array [22].

Because of the small number of the optical antennas and the large antenna spacings, the existing 2D photonic integrated OPAs have small aperture, small beam steering range and wide beam width, which are not suitable for space optical communication. Therefore, increasing the scale of 2D photonic integrated OPA with subwavelength antenna spacing is an urgent problem to be solved. In 1D OPA, the optical antennas can be arranged tightly with subwavelength spacing and the number of the optical antennas can be increased easily. However, with the expansion of the scale of 2D OPA, the antenna spacings increase significantly. This is mainly because the waveguides in optical power dividing network
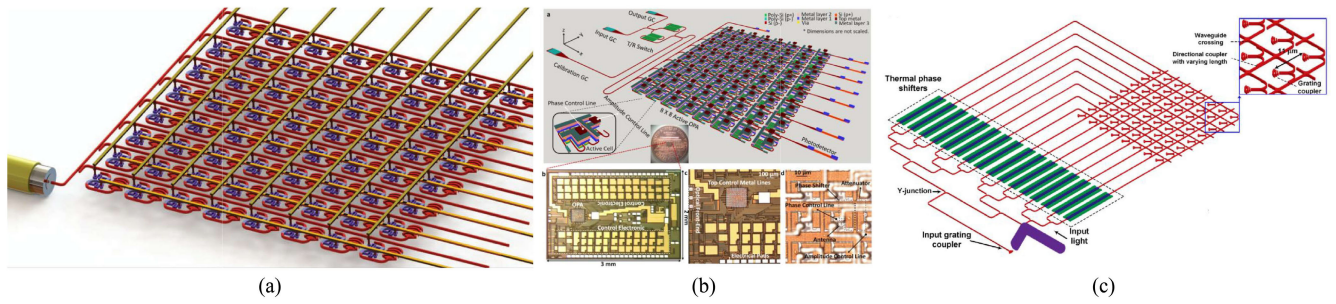
FIGURE 3. Design schemes of 2D OPA. (a) Schematic illustration of the 8 × 8 OPA [19]. (b) Schematic and the microphotograph of the fabricated 8 × 8 monolithic OPA with optical and distinct electrical components [20]. (c) Layout of the 8 × 8 OPA with 16 phase shifters placed outside of the array aperture [21].
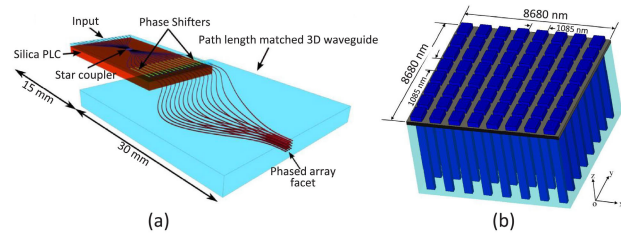

FIGURE 4. Diagrams of (a) the 4 × 4 OPA realized by heterogeneous integration of a 3D waveguide array [24] (b) the 8 × 8 photonic integrated OPA with bottom-feeding hybrid plasmonic nanoantenna [26].

need to occupy a large area between the optical antennas. Therefore, extending a 2D integrated OPA to a huge one with a large number of optical antennas with subwavelength spacings presents a great number of challenges.

There are some novel schemes have also been proposed for achieving large-scale OPA, such as the 2D OPA by adopting high contrast grating (HCG) grating antennas [23], and some end-fire OPAs using 3D waveguide array as emitters [24, 25]. Fig. 4(a) gives the diagram of 4 × 4 end-fire OPA, which is demonstrated by hybrid integration of a 3D waveguide array and a 2D PIC consisting of optical splitter waveguides and waveguide array phase shifters [24]. The 3D waveguide array in the OPA is processed by ultrafast laser inscription. Another large scalable scheme of OPA was proposed by Xu *et al.* [26], as shown in Fig. 4(b). They designed a subwavelength hybrid plasmonic nanoantenna with bottom-feeding. Based on this antenna, a large scalable OPA can be obtained theoretically, but it is still difficult to be fabricated by the current processing technology.

III. THE KEY COMPONENTS OF PHOTONIC INTEGRATED OPA

Fig. 5 shows the schematic diagram of a common silicon integrated OPA chip bonded on PCB with gold wires. As shown in Fig. 5, light is coupled into the silicon waveguide by an optical coupler, and then distributed to the waveguide array by the optical power division network. The optical antenna array is required to radiate light in the waveguide into space. For achieving beam steering, the phase of light in each waveguide is adjusted by the phase shifter, and the voltages loaded on the phase shifters are supplied by a PCB, which is connected with the pads of the phase shifters by gold wires. According to the
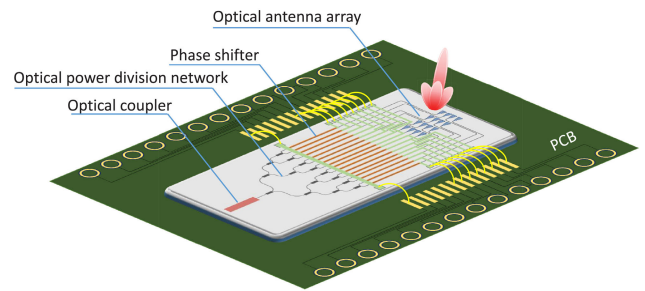

FIGURE 5. Diagram of a silicon integrated optical phased array (OPA) bonded on PCB with gold wires.

principle of field superposition, arbitrary beam pointing can be achieved in a range of $-60°$ to $60°$ by adjusting the phase of light in each waveguide.

A. OPTICAL COUPLER

Optical coupler is a key component of OPA chip for guiding the light in optical fiber into the waveguide on the OPA chip, and vice versa. Edge coupling and surface coupling are two common coupling schemes, as shown in Figs. 6(a) and 6(b), respectively. According to the coupling types, optical couplers can be divided into two categories, namely edge couplers and grating couplers.

Edge coupling is a kind of in-plane coupling. In edge coupling, the core of the optical fiber must be aligned to the waveguide on the chip with submicrometer precision. In a standard single-mode fiber, light is confined within a 10.4 μm mode-field diameter. However, in a single-mode silicon waveguide, the light is strongly confined within a 450 nm × 220 nm silicon core. There is a large mismatch between the single-mode fiber mode and the waveguide mode. If the optical fiber is directly butt-coupled to a silicon waveguide without any mode-matching structures, a 30 dB coupling loss will be caused. Therefore, edge coupler is introduced to reduce this loss in photonic integrated chips. A commonly used edge coupler is inverted taper structure based on mode conversion [27], [28], which increases the size of the optical mode and matches well to the small-core fibers. In order to ensure as much light as possible is coupled into the waveguide, it is necessary to dice the chip accurately and polish the chip facet to optical-grade level. Edge coupler has
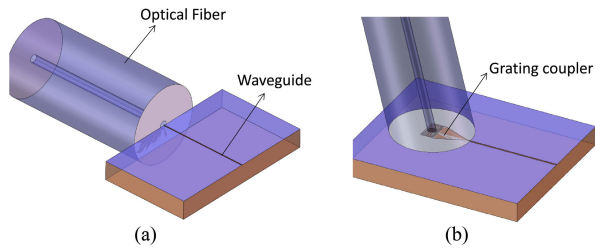
FIGURE 6. Schematic diagrams of (a) edge coupling and (b) surface coupling.

FIGURE 7. Diagrams of (a) parallel and (b) series division network.

the characteristics of broadband and low polarization dependent loss, which makes it ideal for high-performance devices. In order to increase the coupling efficiency, lensed/tapered fibers should be used to confine the light within a small mode-size. However, the cost of lensed/tapered fiber is much higher than that of a typical single-mode fiber. In addition, the steps of accurate dicing and polishing of chip facets also lead to the increase of process complexity and labor cost.

Surface coupling is an out-of-plane coupling. In surface coupling, grating couplers are very common components for coupling light from out-of-plane fibers into waveguides on chips with coupling losses less than 2 dB [29]–[31]. Grating coupler has the advantage of simple fabrication and can be arranged at anywhere on the chip surface. In general, a curved grating followed by an in-plane taper is fabricated on the OPA chip to guide and focus the light into a single-mode waveguide. Although grating coupler can couple light spot with large size into a waveguide efficiently, but it is sensitive to the wavelength and polarization of light. In order to ensure high coupling efficiency, the period of the grating should be redesigned when the wavelength and polarization of the coupled light change.

In practical optical communication applications, OPA chips with these two optical couplers should be packaged to ensure the reliability of the devices. The existing packaging technology is relatively mature for chip packaging.

B. OPTICAL POWER DIVISION NETWORK

Optical power division network is divided into two types of parallel and series division network, as shown in Figs. 7. Parallel division network is a unidirectional extended structure. In parallel division networks, multimode interference (MMI) splitters are important devices for optical power splitting based on the self-imaging principle. Fig. 7(a) shows the diagram of a parallel division network consists of cascaded 1×2 MMI splitters. Usually, the MMIs with symmetrical structure are utilized in OPA to ensure that the phase coincidence and the amplitude equality of the output light. Due to its large size and unidirectionality, the parallel division network is not suitable for 2D array expansion.

Series division network is composed of directional couplers, which are usually composed of two adjacent single-mode waveguides with the spacing of subwavelength. The optical power splitting ratio of the directional coupler is adjusted by the length of the coupling region. As shown in Fig. 7(b), series division network can be extended in two
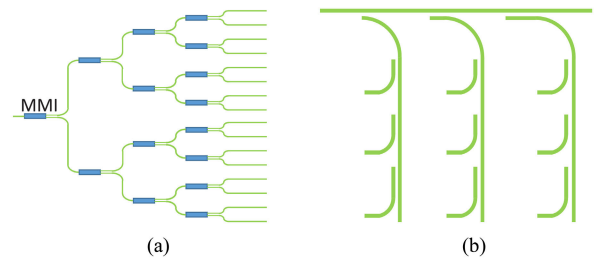
orthogonal directions, which makes the whole optical power dividing network compact.

Directional coupler has the advantages of low transmission loss and easy control of optical power distribution ratio, but it is sensitive to polarization and has small processing parameter allowance. On the contrary, MMI splitter has the advantages of insensitive polarization and good tolerance of process parameters.

The series optical power division network is more suitable for large-scale 2D OPA, but it requires high process accuracy, which is a huge challenge in the chip fabrication. Therefore, directional coupler with high robustness need to be developed in the future.

C. PHASE SHIFTER

Silicon phase shifter is a device for controlling the phase of light, which is the key component to control beam steering in OPA. Silicon phase shifter adjusts the phase of light by changing the refractive index of the silicon waveguide. According to the modulation principle, phase shifters are divided into two types: electro-optic phase shifters based on carrier dispersion effect and thermo-optic phase shifters based on the thermo-optic effect in silicon.

The electro-optic phase shifter works by exploiting the carrier dispersion effect. The real and imaginary parts of the silicon refractive index change as the concentration of free charges in silicon waveguide. The real part of the refractive index is the commonly measured refractive index, and the imaginary part of the refractive index is related to the absorption coefficient of the material. At the wavelength of 1550 nm, the changes of the silicon refractive index Δn and the absorption coefficient $\Delta \alpha$ are evaluated by the variation of the carrier concentrations according to the following formulas [32]

$$\Delta n = \Delta n_e + \Delta n_h = -[8.8 \times 10^{-22} \times \Delta N_e \\ + 8.5 \times 10^{-18} \times (\Delta N_h)^{0.8}], \tag{1}$$

$$\Delta \alpha = \Delta \alpha_e + \Delta \alpha_h = 8.5 \times 10^{-18} \times \Delta N_e \\ + 6.0 \times 10^{-18} \times \Delta N_h, \tag{2}$$

where Δn_e and Δn_h are the changes of the silicon refractive index resulting from the changes of the free-electron and free-hole carrier concentrations, respectively. The parameters of $\Delta \alpha_e$ and $\Delta \alpha_h$ represent the changes of the absorption coefficients resulting from the changes of the free-electron and free-hole carrier concentrations, respectively. The changes
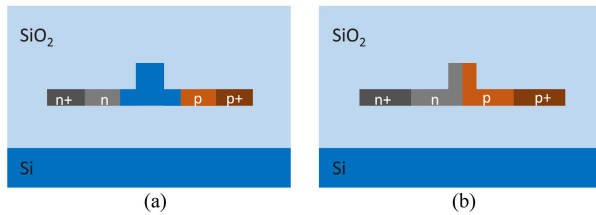
FIGURE 8. Schematic diagram of cross-sections of the electro-optic phase shifters with two typical mechanisms. (a) Carrier injection type (p-i-n junction). (b) Carrier depletion type (p-n junction).

of the free-electron and free-hole carrier concentration are expressed by ΔN_e and ΔN_h, respectively.

Electro-optic phase shifters based on carrier dispersion effect can be divided into carrier injection type (p-i-n junction) and carrier depletion type (p-n junction). Fig. 8 displays the schematic diagrams of cross-sections of the two types of electro-optic phase shifters. In p-i-n phase shifter, doped n- and p-regions are separated by an intrinsic region, which is located in the middle of the waveguide without any doping, as shown in Fig. 8(a). Under forward bias, both free electrons and holes diffuse from high concentration region to intrinsic waveguide region, and the density of the free carrier in the waveguide increases. The carriers are injected into the intrinsic waveguide region by carrier diffusion with high efficiency. However, the injected rate is limited by carrier lifetime, and the carrier diffusion process also leads to optical loss. In p-n phase shifter, the carriers in the waveguide are extracted to form a carrier depletion region under reverse bias, as shown in Fig. 8(b). Therefore, the density of the carriers in the waveguide is changed. The electro-optic phase shifter with this structure can achieve a high modulation speed, which is no longer limited by carrier lifetime. However, due to the small width of depletion region, the efficiency is relatively low. It usually takes a long length to complete a phase shift of π.

The thermo-optic phase shifter is a heater formed by a metal wire above the silicon waveguide or a doping wire in the arm of ridge silicon waveguide. When the voltage is loaded on the heater, the electric power is converted into Joule heat, which results in the temperature of the silicon waveguide rise. The change of temperature in the waveguide causes the change of refractive index allowing for a change of the light phase. Silicon is a material with relatively large thermo-optic coefficient of $\partial n/\partial T = 1.86 \times 10^{-4} \mathrm{K}^{-1}$ at the wavelength of 1550 nm [33]. Since the thermo-optic effect has no influence on the imaginary part of the refractive index of the material, no additional optical loss will be introduced. However, the speed of heat conduction is lower than that of the carrier diffusion, which limits the phase modulation speed of the thermo-optic phase shifter. In addition, the thermo-optic phase shifter has high power consumption because of the good thermal conductivity of silicon and metal.

The properties of a phase shifter include the phase-shifting efficiency, device footprint, phase-shifting range, phase-shifting speed and optical loss. Usually, the power (P_π) required by the phase shifter to achieve a phase shift of π
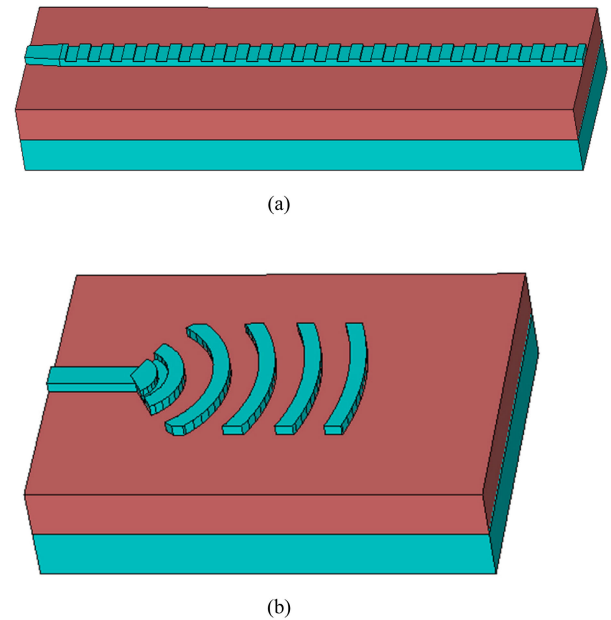

FIGURE 9. Layout of common dielectric grating antennas. (a) Straight waveguide grating antenna. (b) Arc grating antenna.

is used to evaluate the phase-shifting efficiency. A small P_π indicates a high phase-shifting efficiency. Reducing the size of the phase shifter is conducive to achieve a large-scale OPA. Thus, the footprint of the phase shifter should be as small as possible. Phase-shifting range is defined as the phase variation that can be achieved by the phase shifter. In the design of the OPA, phase-shifting range is usually required to be 0-2π. Phase-shifting speed refers to the speed of phase shift, which is related to the mechanisms of the phase shifters. Generally, the electro-optic phase shifter based on carrier dispersion effect has a high phase-shifting speed up to GHz, while the thermo-optic phase shifter has a phase-shifting speed of MHz due to the relatively slow heat conduction speed.

In order to realize large-scale photonic integrated OPA, a phase shifter with large phase-shifting range, high phase-shifting efficiency, small footprint, and low optical loss should be achieved. Recently, attempts have been made to achieve high efficiency, low loss, and compact phase shifters by designing novel geometry structures [13], [34], [35] and combining with some materials with new phase modulating mechanisms, such as germanium [36], [37] and lithium niobate (LiNbO$_3$) [38], [39].

D. OPTICAL ANTENNA
In photonic integrated OPA, optical antenna is a device for converting the light in waveguide to free-propagating optical radiation, and vice versa [40]. The structure, footprint, and radiation properties of optical antenna have a great effect on the far-field radiation pattern of OPA. Silicon grating antennas have been extensively used in photonic integrated OPA. Straight waveguide grating antenna and arc grating antenna are two common silicon grating antennas, as shown in Figs. 9(a) and 9(b), respectively.

Straight waveguide grating antenna is formed by etching periodic slots on silicon waveguide. At the wavelength of 1550 nm, the length of the straight waveguide grating antenna is about hundreds microns, and its width can be less than one wavelength. In most 1D OPA, straight waveguide grating antennas are often used for their narrow width and the ability of beam steering through changing operating wavelength. Narrow width of waveguide grating antenna helps to achieve an antenna array with the smaller antenna spacing. Due to its long length, straight waveguide grating antenna is not suitable for 2D OPA. Arc grating antenna has a footprint of several microns in both dimensions, which is usually used in 2D OPAs [19], [20]. Because of the large footprint, it is difficult to reduce the antenna spacing of the arc grating antenna array to sub-wavelength, which will result in a small beam steering range.

However, there is an unavoidably bidirectional radiation in the silicon grating antenna for the up-down symmetry of their structure. The downward radiation of the optical antenna will reduce the gain of the antenna. Moreover, it will disturb other devices when operating as a transmitter and be disturbed by other devices when operating as a receiver in OPA. In order to improve the upward radiation efficiency of the grating antenna, some solutions have been proposed. By depositing a layer of polysilicon on the top of the silicon grating or introducing a reflection grating at the bottom of grating antenna, the bidirectional radiation will be suppressed and the upward radiation efficiency will be significantly improved [41]–[43].

In order to obtain an optical antenna with high gain and subwavelength footprint, hybrid plasmonic antennas have been proposed [44], [45]. In a hybrid plasmonic antenna, noble metals such as gold and silver are introduced to enhance localized surface plasmon resonance (LSPR). The enhancement of the LSPR leads to an enhanced radiation field of the optical antenna. In 2018, a hybrid plasmonic antenna with bottom-feeding was proposed, which was suitable for constructing a scalable 2D OPA, as shown in Fig. 10(a) [26]. Fig. 10(b) displays the top view of the antenna. The small footprint makes this kind of antennas constitute a compact 2D OPA with a wide range of steering. Fig. 10(c) shows the far-field radiation pattern of the bottom-feeding hybrid plasmonic nanoantenna at 1550 nm. As shown in Fig. 10(c), this kind of optical antenna has no bidirectional radiation, and most of the energy is radiated forward along the direction of the waveguide. However, there are some difficulties in fabrication because of their fine structure and the metal material inside. Therefore, the research on optical antenna with miniaturization, high gain, and easy-to-process should be carried out to pave a way for realizing a large-scalable 2D OPA.

E. OPTICAL ANTENNA ARRAY

The far-field radiation pattern of the antenna array is formed by superposition of the radiation of each antenna. According to the field superposition principle, EMs radiated from
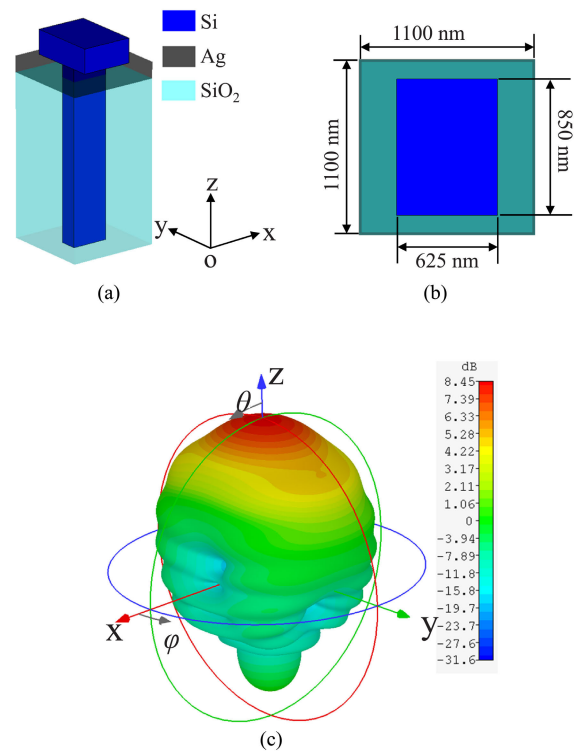

FIGURE 10. (a) Scheme diagram of a hybrid plasmonic antenna [26]. (b) Top view of the hybrid plasmonic antenna [26]. (c) Far-field radiation pattern of the hybrid plasmonic antenna [26].

multiple coherent radiation antennas interfere with each other and superimpose in space. As a result, the radiation intensity of the EM is enhanced in some spatial regions and weakened in other spatial regions, thus the total radiation energy is redistributed in space. The function of optical antenna array is the same as the microwave antenna array. By adjusting the phase of light radiated by each antenna, a beam with high intensity pointing in a specific direction is obtained.

Antenna spacing is defined as the distance between adjacent optical antennas, and it determines the location of grating lobes in the far-field pattern of an antenna array. The appearance of grating lobes will limit the beam steering range of the OPA. In theory, the beam steering angle (ψ_{steer}) of a 1D uniform linear array is given by [46]

$$\sin \psi_{steer} = \frac{\lambda_0 \Delta\phi}{2\pi d}, \qquad (3)$$

where d is the antenna spacing and $\Delta\phi$ represents the phase difference of the fed lights between adjacent antennas. The operating wavelength is expressed by λ_0. Equation (3) shows that when the operating wavelength of the antenna array is fixed, the beam steering angle is determined by the antenna spacing and the phase difference of the light fed into the adjacent antennas. The beam steering range $\Delta\psi_{steer}$ without grating lobes is given by [12]

$$-\sin^{-1}(\frac{\lambda_0}{2d}) < \Delta\psi_{steer} < \sin^{-1}(\frac{\lambda_0}{2d}), \qquad (4)$$

It indicates that smaller antenna spacing will bring a larger beam steering range. For example, when the antenna spacing

is a half-wavelength ($\lambda_0/2$), a wide beam steering range of $-90°$ to $90°$ without grating lobes can be achieved. In addition to beam steering range, beam width is also an important characteristic of the far-field radiation pattern. The beam width of a 1D uniform linear array can be estimated by [47]

$$\Delta\theta \approx \frac{0.886\lambda_0}{Nd\cos\psi_{steer}}, \tag{5}$$

where $\Delta\theta$ represents the full width at half maximum (FWHM) of the main lobe, N is the number of the antennas. Equation (5) shows that the beam width is determined by the aperture of the optical antenna array. A narrow beam can be realized by increasing the number of optical antennas (i.e. a large-scale array) and the optical antenna spacing in the array. Narrow beam is required in space optical communication, and a large beam steering range is conducive to the space communication networking. It is noted that large beam steering range requires small optical antenna spacing, while narrow beam can be reached by large optical antenna spacing. Therefore, it is essential to keep the antenna spacing in an optimal value.

To obtain the far-field pattern of the optical antenna array with both narrow beam and large steering range, nonuniform antenna array is proposed [11]. In nonuniform array, the grating lobes disappear as the periodicity of the array is destroyed. The antenna spacings are usually obtained by some optimization algorithms, such as hill-climbing algorithm, particle swarm optimization (PSO) algorithm [48], and simulated annealing algorithm.

In theory, the radiation pattern of an optical antenna array $F(\theta,\varphi)$ is determined by the product of the array factor and the radiation pattern of the single optical antenna. The calculation formula of the far-field radiation pattern is given by [46]

$$F(\theta,\varphi) = F_e(\theta,\varphi) \cdot S(\theta,\varphi), \tag{6}$$

where $F_e(\theta,\varphi)$ and $S(\theta,\varphi)$ represent the far-field radiation pattern of a single antenna and the array factor, respectively. θ and ϕ represent the azimuth angle and elevation angle, respectively. The array factor of an M $\times$ N rectangular array is determined by

$$S(\theta,\varphi) = \sum_{m=0}^{M-1}\sum_{n=0}^{N-1} I_{mn}e^{j(kd_m\sin\theta\cos\varphi + kd_n\sin\theta\sin\varphi + \alpha_{mn})}, \tag{7}$$

where M and N represent the number of rows and columns in the array, respectively. I_{mn} and α_{mn} are the amplitude and phase of the light radiated from the antenna at mth row and nth column, respectively. d_m and d_n are the position coordinates of the antenna at mth row and nth column, respectively. k is the wave vector.

Since the far-field radiation pattern of a single antenna is fixed, the main effort in antenna array is the design of the array factor, which is determined by the aperture of the optical antenna array and the arrangement of the array. Take 1D array for example, the array factor of the 1D array depends only on the angle θ. Assuming that the optical antennas of the array
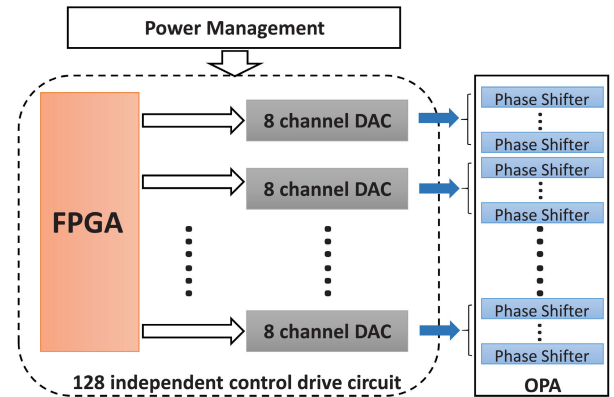

FIGURE 11. Schematic diagram of a DAC based drive control circuit.

are isotropic ($F_e(\theta,\varphi) = 1$), and the wave radiated from each optical antenna has the same amplitude and phase, i.e. $I_{mn} = 1$ and $\alpha_{mn} = 0$, the far-field radiation pattern is simplified to

$$F(\theta) = \sum_{n=0}^{N-1} e^{jkd_n\sin\theta}, \tag{8}$$

In order to obtain the best array arrangement scheme, (8) is used to describe the far-field pattern radiated by a 1D antenna array. Through the optimization algorithm, an antenna position coordinate set of $[d_0, d_1, d_2, \ldots, d_{N-1}]$ is optimized to achieve lowest side lobe when the beam points to 0° ($\theta = 0°$) within the target beam steering range.

F. DRIVE CONTROL CIRCUIT
The drive control circuit is a circuit module used to provide voltage/ current for the phase shifters in OPA. The phase of light is changed by adjusting the voltage/ current loaded on both ends of the phase shifter through the drive control circuit. The drive control circuit can be divided into two categories: one is on the basis of digital-to-analog conversion chip (DAC), and the other is on the basis of analog switch chip.

Fig. 11 shows the schematic diagram of a DAC based control circuit for independent control of 128 channels. The first thing is to select appropriate DAC chips according to phase-shifting characteristics of the phase shifter, such as resistance, voltage/power required for π phase shift. A field programmable gate array (FPGA) chip is used to control 16 high-precision DAC chips with 8 channels, and multichannel voltage/ current signals controlled independently are output by DACs. Then the output voltage/current signals are routed to the respective phase shifters in OPA. In this scheme, the accuracy and refresh rate of the output drive voltage/ current signal depend on the resolution and conversion rate of the DAC chip.

Fig. 12 shows the schematic diagram of an analog switch chip based drive control circuit. In Fig. 12, the reference voltage module is used to generate a square wave voltage reference signal, whose period and amplitude are controlled by the FPGA chip. Then the generated square wave reference signals are modulated by the analog switches that are also controlled by the FPGA chip. Finally, the output voltage
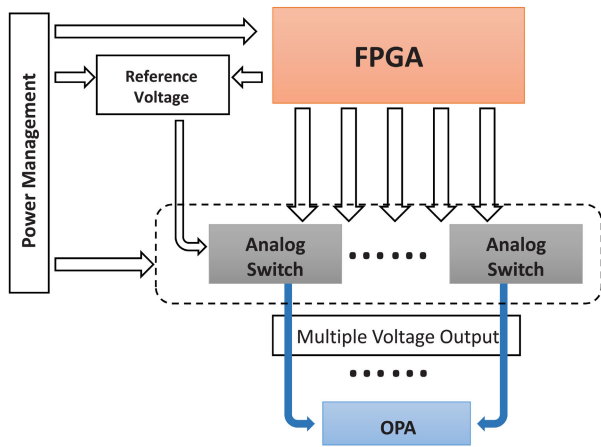
FIGURE 12. Schematic diagram of an analog switch chip based drive control circuit.

FIGURE 13. The experiment setup for the OPA radiation pattern measurement. The red dashed line corresponds to the optical path of far-field imaging, and the green dashed line corresponds to the optical path of near-field intensity distribution without Lens 2.

values are determined by the modulated square wave reference signals, and the output voltage accuracy depends on the operating frequency of the FPGA chip.

With the development of CMOS technology, drive control circuits also can be integrated into a chip. Great progress has been made in low power monolithic integrated circuits for OPA [22]. For a large-scale OPA, it will be the preferred scheme to integrate the photonic and electronic devices on a single chip. In addition, controlling each phase shifter accurately and ensuring the phase synchronization of each channel are also challenging tasks.

IV. PERFORMANCE MEASUREMENT OF OPA

A. FAR-FIELD RADIATION PROPERTIES OF OPA

High directional beams in free space can be formed by controlling the phase of light fed in each of the antennas in OPA individually. The far-field radiation properties of an OPA chip include beam direction, beam width, beam steering range and side-lobe level (SLL). In the far-field radiation pattern, the beam with the maximum intensity is called main lobe, and the other beams with intensity peak are called side lobes. Beam direction refers to the direction of main lobe in free space and is described by beam steering angle. Beam width is equal to the FWHM intensity of the main lobe. The SLL is defined as ten times the logarithm of the ratio of the maximum side lobe intensity to the maximum main lobe intensity, which is determined by

$$SLL = 10\log_{10}(\frac{I_{side-\max}}{I_{main-\max}}), \quad (9)$$

where $I_{side-\max}$ and $I_{main-\max}$ represent the maximum side lobe intensity and maximum main lobe intensity, respectively. Beam steering range refers to the maximum range of the main lobe steering without grating lobes.

B. EXPERIMENT SETUP

The method for measuring the far-field radiation properties of the designed OPA follows the approach proposed by Thomas *et al.* [49]. In the experiment, lens is employed to do the Fourier transform for far-field measurement. The focal
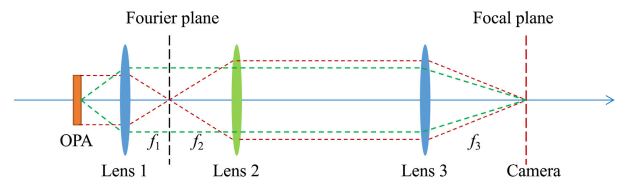
plane of a lens is the Fourier-transform plane. On the Fourier-transform plane, far-field radiation pattern of the OPA can be captured theoretically. The experiment setup consists of three achromatic lenses and an infrared camera, as shown in Fig. 13. The focal lengths of the three achromatic lenses are f_1, f_2, and f_3, respectively. In principle, the far field radiated by OPA appears on the focal plane of Lens 1. The other two lenses L1 and L2 are used to enlarge the far-field radiation pattern. Lens 2 and Lens 3 form a telescope system with the magnification of f_3/f_2. An InGaAs camera is placed on the focal plane of Lens 3 to capture the far-field intensity distribution. By removing Lens 2, the near-field radiation pattern is measured. In Fig. 13, the red and green dashed lines represent the optical path of far-field and near-field imaging, respectively. The relative positions among the OPA chip under test, the detection plane and three lenses are given in Fig. 13 clearly. The distance between Lens 1 and Lens 2 is $f_1 + f_2$, and the distance between Lens 3 and the detection surface of camera is f_3.

In this experiment setup, the radiation field of the OPA is collected by Lens 1 directly. Lens with large numerical aperture (NA) helps to obtain a far field with wide range. Therefore, an achromatic lens with the largest NA should be chosen as Lens 1. The focal lengths of Lens 2 and Lens 3 should be selected according to the required magnification. Because of the limitation of camera detection area, the magnification should be not too large. In our test, an aspheric lens with high NA of 0.55 and focal length of 10 mm is selected as Lens1, i.e., NA = 0.55 and f_1 = 10 mm. Two achromatic lenses with focal lengths of 75 mm and 100 mm are chosen as Lens 2 and Lens 3, respectively, i.e., f_2 = 75 mm and f_3 = 100 mm. Thus, the magnification is about 1.33. An InGaAs camera with 640×512 pixels and 20 μm pitch is utilized to capture the field distribution. The maximum angle measurable by the system is $51.2° \times 42°$ with a resolution of $0.09°$ in two orthogonal directions.

V. A PROOF-OF-CONCEPT: 1 × 64 NONUNIFORM SILICON INTEGRATED OPA.

In order to verify the feasibility of the OPA design and test process mentioned above, a silicon integrated OPA with 1×64 nonuniform antenna array is designed and measured as a proof-of-concept. The operating wavelength of the OPA is 1550 nm, i.e. λ = 1550 nm. Fig. 14(a) presents the design layout of the OPA chip. The OPA is fabricated on a SOI wafer, which has a 220 nm top silicon layer on a 2 μm buried

silicon-dioxide layer. The designed OPA contains a grating coupler, a parallel optical power division network, 64 thermo-optic phase shifters and 64 straight waveguide grating antennas. In the parallel division network, 63 cascaded 1 × 2 MMI are used to split the light into 64 equal channels. The thermo-optic phase shifters are titanium nitride (TiN) resistor wires with length of 150 μm and width of 3 μm, and they are placed 1 μm above the silicon waveguides. Each phase shifter has a resistance of 1.2 kΩ. The straight waveguide grating antennas have 400 μm length, 600 nm width, and 50% duty cycle. The grating pitch is 650 nm, and the etching depth of the grating antenna is 150 nm, which is chosen to ensure high upward radiation efficiency. The antenna spacings of the nonuniform grating antenna array are optimized by using PSO algorithm. In the optimization process, we take the beam steering range of ±14° as the optimization goal, and make the SLL of the far-field radiation pattern in this range reach the minimum value. The optimization range of each of the antenna spacings is set from 2λ to 5λ (λ = 1550 nm), and the aperture of the antenna array is set to 320 μm. The best antenna spacing distribution is optimized by multiple iterations. In each iteration, the SLL is calculated as the evaluation function. It is assumed that the excitation in each antenna has the same amplitude of 1 and the same phase of 0. The far-field radiation pattern of the array and the SLL are calculated by using (8) and (9), respectively. After 2000 iterations of the optimization, 63 nonuniform optical antenna spacings are obtained with a maximum value of 6.349 μm and a minimum value of 3.1 μm. The antenna spacing distribution in the antenna array is shown in Fig. 14(b).

Fig. 15 displays the optical image of the fabricated OPA mounted on a PCB. In Fig. 15, the designed OPA with AlCu wires is enclosed in a red box. The AlCu wires connecting pads and phase shifters are used to supply power to the phase shifters. The fabricated OPA chip is mounted on a PCB, and the pads of the phase shifters in the chip are connected with the electrodes on the PCB by gold wire bonding. The PCB is mounted on a copper heat sink and its backside is metalized for thermal conduction. To maintain a constant temperature for the OPA chip, a thermoelectric cooler (TEC) element and a temperature transducer are embedded in the heat sink, which are controlled by a temperature controller. A commercial voltage analog output module provided by National Instruments (NI) Company, NI-PXle-6739, is connected to the pins on the PCB to provide DC voltage for each phase shifter in the OPA.

In the experiment, a 1550 nm continuous light is output by a tunable semiconductor laser. A standard fiber with flat end face is used to couple the light into the OPA chip through a grating coupler. The light is divided into 64 waveguide channels and is radiated into the free space via 64 long straight waveguide grating antennas. A Hamamatsu C12741-03 IR camera is used in the experiment setup to receive the far-field radiation pattern of the OPA chip. By adjusting the phase shifters, the beam steering is achieved in the direction of θ as shown in Fig. 14(a). The PSO algorithm combing with
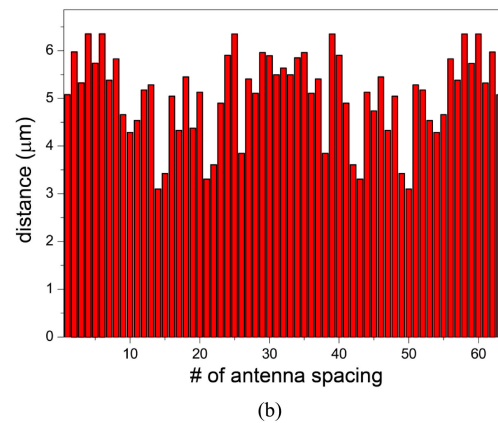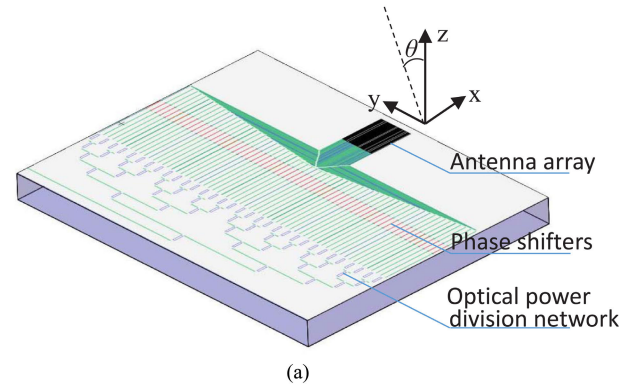

(a)

(b)

FIGURE 14. (a) Design layout of the 1 × 64 OPA with nonuniform optical antennas. (b) Calculated 63 antenna spacings of the designed nonuniform array.
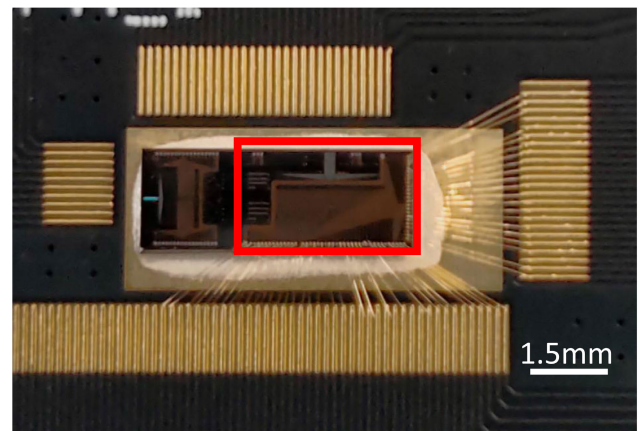

FIGURE 15. Optical image of the fabricated OPA mounted on a PCB.

the feedback from the IR camera is utilized to optimize the voltage in each phase shifter for beam pointing to a given direction. Through hundreds of iterations, a desired far-field pattern with preset beam direction is obtained. In the angle range from −14° to +14°, 29 beam directions with the angle interval of 1° are achieved by the optimizing voltage sets. Some of the measured 3D far-field radiation patterns of the designed 1 × 64 OPA are displayed in Fig. 16. It is clearly
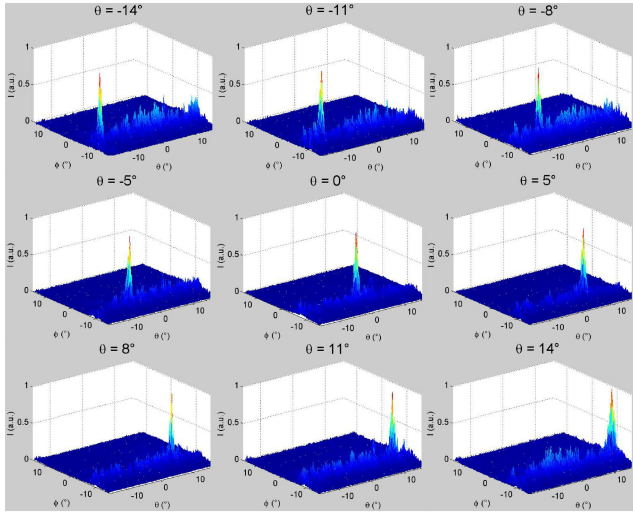
FIGURE 16. Experimental results of the 3D far-field radiation pattern of the designed 1 × 64 OPA steering from −14° to 14°.
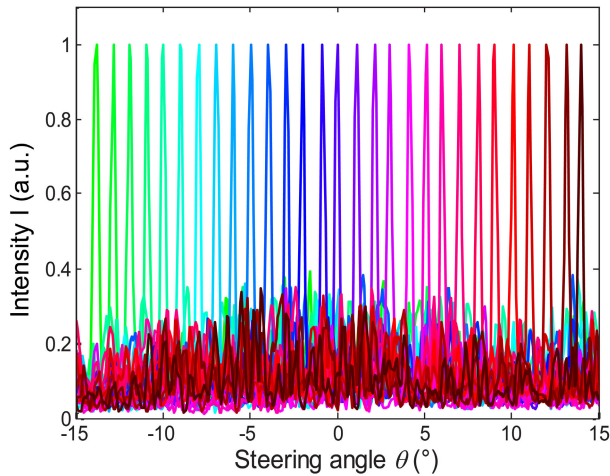

FIGURE 17. Experimental results of the 2D far-field radiation pattern of the designed OPA steering from −14° to 14° with the interval of 1°.

seen that the beam steers in the θ dimension without grating lobes. To further investigate the beam steering properties, we extract the normalized 2D far-field radiation pattern along the steering direction, as shown in Fig. 17.

The numerical simulation analysis of the far-field radiation properties of the designed 1 × 64 nonuniform antenna array is performed. In the simulation, it is assumed that the wave radiated by each optical antenna has the same amplitude and different phase. Thus, the far-field radiation pattern of the optical antenna array (7) can be written as

$$S(\theta) = \sum_{n=0}^{63} e^{j(kd_n \sin\theta + \alpha_n)}, \qquad (10)$$

which is taken as the objective of the phase optimization. In (10), we set the first optical antenna at the coordinate origin, i.e., $d_0 = 0$. The other optical antenna coordinates d_n are obtained according to the designed antenna spacings in Fig. 14(b). After the same number of iterations as in the
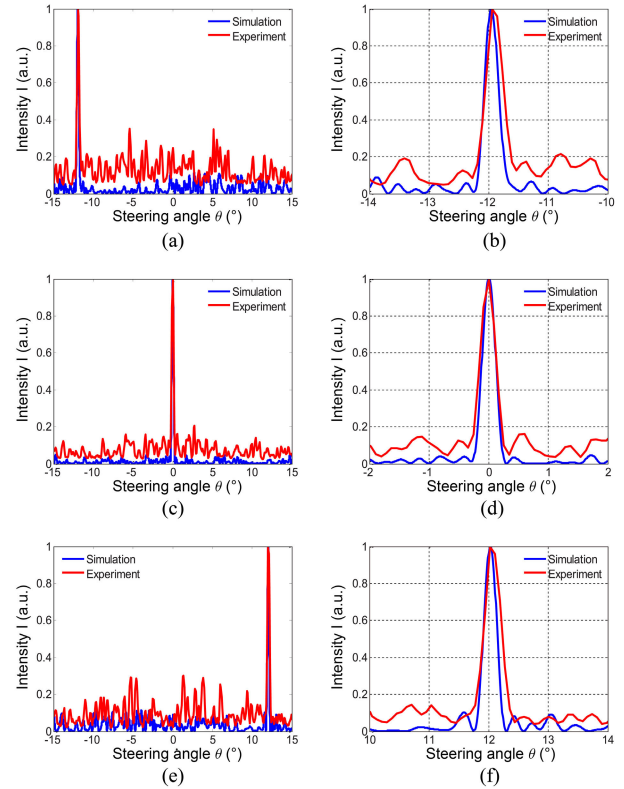

FIGURE 18. Normalized 2D far-field radiation pattern in the θ direction. (a) $\theta = -12°$, (c) $\theta = 0°$, and (e) $\theta = 12°$, respectively. Partially enlarged 2D far-field radiation pattern near the main lobe for the beam directions of (b) $\theta = -12°$, (d) $\theta = 0°$, and (f) $\theta = 12°$, respectively.

experiment, a set of phase values $[\alpha_0, \alpha_1, \ldots, \alpha_{63}]$ corresponding to the beam direction of θ is obtained by the optimization algorithm. When we plug these phase values into (10), the far-field radiation pattern of the OPA is obtained.

Because the phase values obtained by PSO algorithm are randomly distributed, the phase values in the simulation and the measurement cannot be compared directly. We compare the measured and simulated far-field radiation patterns of the OPA for the preset beam direction of $\theta = -12°$, $\theta = 0°$, and $\theta = 12°$, as shown in Fig. 18. Both of the simulated and measured 2D far-field radiation patterns with beam direction of $\theta = -12°$, $\theta = 0°$, and $\theta = 12°$ are displayed in Figs. 18(a), (c), (e), respectively. For a clearer comparison, the 2D far-field radiation patterns near their respective main lobes are displayed in Figs. 18(b), (d), (f), respectively. The red and blue curves represent the experimental and simulated results, respectively. The experimental results show that the measured beam directions are −11.94°, 0°, and 12.02°, respectively. In Figs. 18(b), (d), and (e), the measured beam widths of the main lobe are 0.25°, 0.17°, and 0.25°, respectively. In the simulation, the calculated beam directions are −11.96°, 0°, and 12.03°, respectively. The calculated beam widths of the main lobe at the three directions are 0.26°, 0.25°, and 0.24°, respectively. It can be found that the measured far-field radiation patterns are in good agreement with the simulated results. The measured SLL is higher than the

simulation value due to the limited dynamic range and the background noise of the camera. Although the beam steering range of the designed 1 × 64 OPA chip is only 28°, the beam width is about 0.25°, which is far less than the reported beam width 1.6° of the OPA with 64 emitters [17].

VI. CONCLUSION AND DISCUSSION

In conclusion, we reviewed the development of photonic integrated monolithic OPA in recent years. The design scheme of the key components in the silicon integrated OPA, including optical coupler, optical power division network, phase shifter, optical antenna has been summarized. The design methods of optical antenna array and the drive control circuit for beam steering have been discussed. We have provided the experiment setup and test method for detecting the far-field radiation pattern of the OPA chip. In order to prove the feasibility of the design and test methods of the OPA we summarized, a silicon integrated OPA with 1×64 nonuniform antenna array has been demonstrated as a proof-of-concept, and the far-field radiation properties of the OPA chip have also been investigated in detail. The measured results are basically consistent with the simulation results, and it shows the validity of the OPA chip design scheme.

According to the principle of reciprocity of light, the optical antenna array in OPA can not only radiate the beam, but also receive the beam from a certain direction. It enables OPA chips replace the heavy receiving and transmitting modules in space optical communication. However, in the practical application, there are still some challenges in some aspects, such as the radiation optical power, beam loss, power consumption, and array scale, of the silicon integrated OPA chip.

Silicon has a strong nonlinear absorption effect. In silicon waveguide, the nonlinear effects, such as Kerr effect, two-photon absorption, four-wave mixing, *et al.* will become significant as the optical power increases. For a typical 220 nm SOI waveguide, the optical power should not be larger than a few hundred mW [50]. Therefore, monolithic silicon integrated OPA cannot directly meet the requirement of the long-distance space optical communication. An alternative solution is to replace the silicon by a low-loss material of silicon nitride (SiN) [51]. Compared with silicon waveguide, SiN waveguide allows orders of magnitude higher optical power without significant nonlinear effect.

In an OPA chip, the losses of beam result from the optical coupling loss, the silicon waveguide loss, and the optical division loss. According to [52], for 1550 nm wavelength, the propagation loss of the 220 nm-thick Si waveguide is less than 0.5 dB/cm, and the loss of a 1 × 2 Si MMI splitter is about 0.1dB. We take the OPA with 16384 (2^{14}) optical antennas as an example to analyze the beam losses. A single waveguide is split into 16384 channels by utilizing the 1 × 2 MMI 14 times, and an additional splitting loss of 1.4 dB is resulted in. Assuming that the light propagates 1 cm in the waveguide, a propagation loss of 0.5 dB is caused. Due to the bidirectional radiation of the dielectric grating antennas, only 50% of the optical power will be radiated. Thus, if the

light with 100 mW is fed into the input waveguide of the OPA, about 32 mW optical power will be concentrated on the main lobe. It is necessary to further reduce loss and improve the radiation power of the OPA to achieve a longer-range communication.

Meanwhile, the power consumption of an OPA with thousands of phase shifters will be extremely high. With the expansion of the phase shifters in large-scale OPA, more and more electrical components are used in the drive control circuit, which will lead to huge power consumption and volume of the drive control circuit.

Another major challenge of the development of the silicon integrated OPA is 2D large-scale expansion. Nowadays, due to the small-scale of the OPA chip, the application for OPA in space optical communication is limited. As the number of optical antennas and phase shifters increase, the optical power division network and the pads of the phase shifter require larger area. These issues result in a large optical antenna spacing which leads to grating lobes and limits beam steering range. Perhaps the 3D PIC technology is a potential way to achieve a large-scale OPA chip.

Therefore, it is essential to carry out some researches on miniaturized optical antenna with high gain, optical phase shifter with high speed and low power consumption, and compact optical power division network with low loss. Additionally, some new schemes for building a large-scalable 2D array should be given sufficient consideration and studied in depth.

ACKNOWLEDGMENT

REFERENCES
[1] M. Yu, Y. Li, J. Pang, D. Kong, Z. Yang, and J. Wu, "Highly power-efficient Nyquist-mPPM-LQAM modulation with enhanced spectrum efficiency," *IEEE Photon. Technol. Lett.*, vol. 29, no. 1, pp. 94–97, Jan. 1, 2017.

[2] J. F. Algorri, G. D. Love, and V. Urruchi, "Modal liquid crystal array of optical elements," *Opt. Express*, vol. 21, no. 21, pp. 24809–24818, Oct. 2013.

[3] D. P. Resler, D. S. Hobbs, R. C. Sharp, L. J. Friedman, and T. A. Dorschner, "High-efficiency liquid-crystal optical phased-array beam steering," *Opt. Lett.*, vol. 21, no. 9, pp. 689–691, May 1996.

[4] L. Wu, X. Wang, X. He, Z. Huang, X. Huang, and C. Xiong, "Arbitrary multiple beam forming by two cascaded liquid crystal optical phased arrays," *Opt. Express*, vol. 26, no. 13, pp. 17066–17077, Jun. 2018.

[5] Y. Wang, G. Zhou, X. Zhang, K. Kwon, P. A. Blanche, N. Triesault, K.-S. Yu, and M. C. Wu, "2D broadband beamsteering with large-scale MEMS optical phased array," *Optica*, vol. 6, no. 5, pp. 557–562, May 2019.

[6] W. Yang, T. Sun, Y. Rao, M. Megens, T. Chan, B.-W. Yoo, D. A. Horsley, M. C. Wu, and C. J. Chang-Hasnain, "High speed optical phased array using high contrast grating all-pass filters," *Opt. Express*, vol. 22, no. 17, pp. 20038–20044, Aug. 2014.

[7] B. W. Yoo, M. Megens, T. Chan, T. Sun, W. Yang, C. J. Chang-Hasnain, D. A. Horsley, and M. C. Wu, "Optical phased array using high contrast gratings for two dimensional beamforming and beamsteering," *Opt. Express*, vol. 21, no. 10, pp. 12238–12248, May 2013.

[8] B. W. Yoo, M. Megens, T. Sun, W. Yang, C. J. Chang-Hasnain, D. A. Horsley, and M. C. Wu, "A 32 × 32 optical phased array using polysilicon sub-wavelength high-contrast-grating mirrors," *Opt. Express*, vol. 22, no. 16, pp. 19029–19039, Aug. 2014.

[9] K. Van Acoleyen, W. Bogaerts, and J. Jágerská, N. Le Thomas, R. Houdré, and R. Baets, "Off-chip beam steering with a one-dimensional optical phased array on silicon-on-insulator," *Opt. Lett.*, vol. 34, no. 9, pp. 1477–1479, May 2009.

[10] C. V. Poulton, A. Yaccobi, Z. Su, M. J. Byrd, and M. R. Watts, "Optical phased array with small spot size, high steering range and grouped cascaded phase shifters," in *Proc. Adv. Photon. (IPR, NOMA, Sensors, Netw., SPPCom, SOF)*, Vancouver, BC, Canada, 2016, pp. 1–3.

[11] D. N. Hutchison, J. Sun, J. K. Doylend, R. Kumar, J. Heck, W. Kim, C. T. Phare, A. Feshali, and H. Rong, "High-resolution aliasing-free optical beam steering," *Optica*, vol. 3, no. 8, pp. 887–890, Aug. 2016.

[12] S. Chung, H. Abediasl, and H. Hashemi, "A monolithically integrated large-scale optical phased array in Silicon-on-Insulator CMOS," *IEEE J. Solid-State Circuits*, vol. 53, no. 1, pp. 275–296, Jan. 2018.

[13] S. A. Miller, Y. C. Chang, C. T. Phare, M. C. Shin, M. Zadka, S. P. Roberts, B. Stern, X. Ji, A. Mohanty, O. A. J. Gordillo, and U. D. Dave, "Large-scale optical phased array using a low-power multi-pass silicon photonic platform," *Optica*, vol. 7, no. 1, pp. 3–6, Jan. 2020.

[14] W. Guo, P. R. A. Binetti, C. Althouse, M. L. Masanovic, H. P. M. M. Ambrosius, L. A. Johansson, and L. A. Coldren, "Two-dimensional optical beam steering with InP-based photonic integrated circuits," *IEEE J. Sel. Topics Quantum Electron.*, vol. 19, no. 4, p. 6100212, Jul. 2013.

[15] J. C. Hulme, J. K. Doylend, M. J. R. Heck, J. D. Peters, M. L. Davenport, J. T. Bovington, L. A. Coldren, and J. E. Bowers, "Fully integrated hybrid silicon two dimensional beam scanner," *Opt. Express*, vol. 23, no. 5, pp. 5861–5874, Mar. 2015.

[16] Y. Zhang, K. Shang, Y.-C. Ling, and S. J. Ben Yoo, "3D integrated silicon photonic unit cell with vertical U-turn for scalable optical phase array," in *Proc. Conf. Lasers Electro-Optics*, San Jose, CA, USA, 2018, pp. 1–2.

[17] C. T. Phare, M. Chul Shin, S. A. Miller, B. Stern, and M. Lipson, "Silicon optical phased array with high-efficiency beam formation over 180 degree field of view," 2018, *arXiv:1802.04624*. [Online]. Available: http://arxiv.org/abs/1802.04624

[18] K. Van Acoleyen, H. Rogier, and R. Baets, "Two-dimensional optical phased array antenna on silicon-on-insulator," *Opt. Express*, vol. 18, no. 13, pp. 13655–13660, Jun. 2010.

[19] J. Sun, E. Timurdogan, A. Yaacobi, E. S. Hosseini, and M. R. Watts, "Large-scale nanophotonic phased array," *Nature*, vol. 493, no. 7431, pp. 195–199, Jan. 2013.

[20] H. Abediasl and H. Hashemi, "Monolithic optical phased-array transceiver in a standard SOI CMOS process," *Opt. Express*, vol. 23, no. 5, pp. 6509–6519, Mar. 2015.

[21] F. Ashtiani and F. Aflatouni, "N × N optical phased array with 2N phase shifters," *Opt. Express*, vol. 27, no. 19, pp. 27183–27190, Sep. 2019.

[22] R. Fatemi, A. Khachaturian, and A. Hajimiri, "A nonuniform sparse 2-D large-FOV optical phased array with a low-power PWM drive," *IEEE J. Solid-State Circuits*, vol. 54, no. 5, pp. 1200–1215, May 2019.

[23] P. Wang, G. Luo, Y. Li, M. Wang, F. Meng, W. Yang, H. Yu, X. Zhou, Y. Zhang, and J. Pan, "Two-dimensional large-angle scanning optical phased array with single wavelength beam," in *Proc. Conf. Lasers Electro-Optics*, San Jose, CA, USA, 2019, pp. 1–2.

[24] B. Guan, C. Qin, R. P. Scott, B. Ercan, N. K. Fontaine, T. Su, and S. J. B. Yoo, "Hybrid 3D photonic integrated circuit for optical phased array beam steering," in *Proc. CLEO*, San Jose, CA, USA, 2015, pp. 1–2.

[25] S. J. B. Yoo, B. Guan, and R. P. Scott, "Heterogeneous 2D/3D photonic integrated microsystems," *Microsyst. Nanoeng.*, vol. 2, no. 1, p. 16030, Dec. 2016.

[26] Y. Xu, T. Dong, J. He, and Q. Wan, "Large scalable and compact hybrid plasmonic nanoantenna array," *Opt. Eng.*, vol. 57, no. 8, p. 087101, Aug. 2018.

[27] T. Shoji, T. Tsuchizawa, T. Watanabe, K. Yamada, and H. Morita, "Low loss mode size converter from 0.3 μm square Si wire waveguides to single-mode fibers," *Electron. Lett.*, vol. 38, no. 25, pp. 1669–1670, Dec. 2002.

[28] V. R. Almeida, R. R. Panepucci, and M. Lipson, "Nanotaper for compact mode conversion," *Opt. Lett.*, vol. 28, no. 15, pp. 1302–1304, Aug. 2003.

[29] F. Van Laere, G. Roelkens, M. Ayre, J. Schrauwen, D. Taillaert, D. Van Thourhout, T. F. Krauss, and R. Baets, "Compact and highly efficient grating couplers between optical fiber and nanophotonic waveguides," *J. Lightw. Technol.*, vol. 25, no. 1, pp. 151–156, Jan. 2007.

[30] J. V. Galan, P. Sanchis, J. Blasco, and J. Marti, "Study of high efficiency grating couplers for silicon-based horizontal slot waveguides," *IEEE Photon. Technol. Lett.*, vol. 20, no. 12, pp. 985–987, Jun. 2008.

[31] J. S. Yang, O. Beom-Hoan, S. H. Hong, S. G. Lee, S.-G. Park, J.-H. Kim, D.-J. Chung, S.-P. Chang, and E.-H. Lee, "Novel grating design for out-of-plane coupling with nonuniform duty cycle," *IEEE Photon. Technol. Lett.*, vol. 20, no. 9, pp. 730–732, May 2008.

[32] R. Soref and B. Bennett, "Electrooptical effects in silicon," *IEEE J. Quantum Electron.*, vol. 23, no. 1, pp. 123–129, Jan. 1987.

[33] R. Soref and J. Larenzo, "All-silicon active and passive guided-wave components for λ= 1.3 and 1.6 μm," *IEEE J. Quantum Electron.*, vol. 22, no. 6, pp. 873–879, Jun. 1986.

[34] S. Chung, M. Nakai, and H. Hashemi, "Low-power thermo-optic silicon modulator for large-scale photonic integrated systems," *Opt. Express*, vol. 27, no. 9, pp. 13430–13459, Apr. 2019.

[35] A. Densmore, S. Janz, R. Ma, J. H. Schmid, D.-X. Xu, A. Delâge, J. Lapointe, M. Vachon, and P. Cheben, "Compact and low power thermo-optic switch using folded silicon waveguides," *Opt. Express*, vol. 17, no. 13, pp. 10457–10465, Jan. 2009.

[36] J. E. Roth, O. Fidaner, E. H. Edwards, R. K. Schaevitz, Y.-H. Kuo, N. C. Helman, T. I. Kamins, J. S. Harris, and D. A. B. Miller, "C-band side-entry Ge quantum-well electroabsorption modulator on SOI operating at 1 V swing," *Electron. Lett.*, vol. 44, no. 1, pp. 49–50, Jan. 2008.

[37] J. E. Roth, O. Fidaner, R. K. Schaevitz, Y. H. Kuo, T. I. Kamins, J. S. Harris, and D. A. B. Miller, "Optical modulator on silicon employing germanium quantum wells," *Opt. Express*, vol. 15, no. 9, pp. 5851–5859, Apr. 2007.

[38] C. Wang, M. Zhang, X. Chen, M. Bertrand, A. Shams-Ansari, S. Chandrasekhar, P. Winzer, and M. Lončar, "Integrated lithium niobate electro-optic modulators operating at CMOS-compatible voltages," *Nature*, vol. 562, no. 7725, pp. 101–104, Oct. 2018.

[39] M. Zhang, B. Buscaino, C. Wang, A. Shams-Ansari, C. Reimer, R. Zhu, J. M. Kahn, and M. Lončar, "Broadband electro-optic frequency comb generation in a lithium niobate microring resonator," *Nature*, vol. 568, no. 7752, pp. 373–377, Apr. 2019.

[40] P. Bharadwaj, B. Deutsch, and L. Novotny, "Optical antennas," *Adv. Opt. Photon.*, vol. 1, no. 3, pp. 438–483, Aug. 2009.

[41] G. Roelkens, D. V. Thourhout, and R. Baets, "High efficiency Silicon-on-Insulator grating coupler based on a poly-Silicon overlay," *Opt. Express*, vol. 14, no. 24, pp. 11622–11630, Nov. 2006.

[42] Y. Xu, T. Dong, and H. Zhao, "Utilizing a novel configuration for side-lobes suppression of a dielectric optical nanoantenna," in *Proc. Int. Top. Meeting Microw. Photon. (MWP)*, Beijing, China, Oct. 2017, pp. 1–3.

[43] Y. Xu, T. Dong, and H. Zhao, "A novel miniaturized dielectric optical nanoantenna," in *Proc. Asia Commun. Photon. Conf.*, Guangdong, China, 2017, pp. 1–3.

[44] B. A. Nia, L. Yousefi, and M. Shahabadi, "Integrated optical-phased array nanoantenna system using a plasmonic rotman lens," *J. Lightw. Technol.*, vol. 34, no. 9, pp. 2118–2126, May 1, 2016.

[45] L. Yousefi and A. C. Foster, "Waveguide-fed optical hybrid plasmonic patch nano-antenna," *Opt. Express*, vol. 20, no. 16, pp. 18326–18335, Jul. 2012.

[46] J. L. Volakis, R. C. Johnson, H. Jasik, and T. F. Eibert, *Antenna Engineering Handbook*. New York, NY, USA: McGraw-Hill, 2007.

[47] P. F. McManamon, T. A. Dorschner, D. L. Corkum, L. J. Friedman, D. S. Hobbs, M. Holz, S. Liberman, H. Q. Nguyen, D. P. Resler, R. C. Sharp, and E. A. Watson, "Optical phased array technology," *Proc. IEEE*, vol. 84, no. 2, pp. 268–298, Feb. 1996.

[48] J. Robinson and Y. Rahmat-Samii, "Particle swarm optimization in electromagnetics," *IEEE Trans. Antennas Propag.*, vol. 52, no. 2, pp. 397–407, Feb. 2004.

[49] N. Le Thomas, R. Houdré, M. V. Kotlyar, D. O'Brien, and T. F. Krauss, "Exploring light propagating in photonic crystals with Fourier optics," *J. Opt. Soc. Amer. B, Opt. Phys.*, vol. 24, no. 12, pp. 2964–2971, Dec. 2007.

[50] X. Sun, L. Zhang, Q. Zhang, and W. Zhang, "Si photonics for practical LiDAR solutions," *Appl. Sci.*, vol. 9, no. 20, p. 4225, Oct. 2019.

[51] P. Wang, G. Luo, Y. Xu, Y. Li, Y. Su, J. Ma, R. Wang, Z. Yang, X. Zhou, Y. Zhang, and J. Pan, "Design and fabrication of a SiN-Si dual-layer optical phased array chip," *Photon. Res.*, vol. 8, no. 6, p. 912, 2020.

[52] T. Mogami, T. Horikawa, K. Kinoshita, H. Sasaki, K. Morito, and K. Kurata, "A 300 mm Si photonics platform for optical interconnection," in *Proc. IEEE Int. Interconnect Technol. Conf. IEEE Mater. for Adv. Metallization Conf. (IITC/MAM)*, Grenoble, France, May 2015, pp. 273–276.

JINGWEN HE received the B.S. degree in physics and the M.S. degree in optics from Capital Normal University, Beijing, China, in 2010 and 2013, respectively, and the Ph.D. degree in physics from the Harbin Institute of Technology, Harbin, China, in 2017. She is currently an Engineer with the State Key Laboratory of Space-Ground Integrated Information Technology, Beijing Institute of Satellite Information Engineering. Her research interests include metasurface, terahertz field modulation, optical antenna, and silicon photonic device.

YUE XU received the B.S. degree in electronic science and technology from the University of Yanshan, Qinhuangdao, China, in 2015, and the M.S. degree in information and communication engineering from the State Key Laboratory of Space-Ground Integrated Information Technology, Beijing Institute of Satellite Information Engineering, Beijing, China, in 2018. He is currently an Engineer with the State Key Laboratory of Space-Ground Integrated Information Technology, Beijing Institute of Satellite Information Engineering. His research interests include design, simulation, and measurement of optical nanoantennas and phased arrays.

• • •

TAO DONG received the B.S. and Ph.D. degrees in electronics science and technology from the Beijing Institute of Technology, in 1999 and 2004, respectively. He is currently a Professor with the State Key Laboratory of Space-Ground Integrated Information Technology, Beijing Institute of Satellite Information Engineering. His research interests include antenna, phased array, optoelectronic devices, and free space optical communication.